Research Group in Microfluidic & Photoelectrocatalytic Engineering
Chemical Engineering Department
Centro Universitário FEI

Photocatalytic Ammonia Synthesis from Nitrogen in Water using Iron Oxides: Comparative Efficiency of Goethite, Magnetite, and Hematite

Cátia Alexandra Podence Alves [1], Priscila Hasse Palharim[2], Bruna Pratto[3], Andre Luiz da Silva[1], Douglas Gouvêa[1], Bruno Ramos[3,*]

[1]*Department of Metallurgical and Materials Engineering, Escola Politécnica, University of São Paulo, São Paulo, 05508-010, Brazil*

[2]*Center for Natural and Human Sciences, Federal University of ABC, 09210-580, Santo André, Brazil*

[3]*Microfluidic & Photoelectrocatalytic Engineering Lab. Department of Chemical Engineering, Centro Universitário FEI, São Bernardo do Campo, SP, Brazil*

***CORRESPONDING AUTHOR:**

Bruno Ramos – brunoramos@fei.edu.br

Abstract. Photocatalytic ammonia synthesis from nitrogen and water presents a promising pathway for decentralized sustainable ammonia production, leveraging the abundant solar energy. In this study, we explore the efficacy of three iron oxide polymorphs – goethite (α-FeO(OH)), magnetite (Fe_3O_4), and hematite (α-Fe_2O_3) – as photocatalysts for nitrogen reduction under ultraviolet (UV) light. The materials were synthesized using hydrothermal and polymeric precursor methods, characterized by X-ray diffraction (XRD), scanning electron microscopy (SEM), diffuse reflectance infrared Fourier transform spectroscopy (DRIFTS), UV-Vis spectroscopy, photoluminescence spectroscopy, and thermal analysis to understand their structural, surface, and optoelectronic properties. Among the materials tested, goethite demonstrated the highest ammonia production rate (20.6 μmol g^{-1} h^{-1}), which we attribute to its larger specific surface area and the stability of its surface hydroxyl groups, which play a critical role in facilitating the protonation and electron transfer necessary for nitrogen reduction. Curiously, magnetite also displayed some activity (10.3 μmol g^{-1} h^{-1}), likely due to the formation of a heterojunction with the co-occurring goethite phase. Hematite showed the fastest area-based production rate (1.05 μmol m^{-2} h^{-1}), suggesting it is the polymorph with highest density of active sites for N_2 reduction. This work contributes to the ongoing search for greener and lower-cost alternatives to the Haber-Bosch process, with implications for both agriculture and energy storage.

Keywords: Photocatalysis; Ammonia; Iron Oxides; Goethite; Hematite; Magnetite.

1. INTRODUCTION

Ammonia is the second most-produced synthetic chemical worldwide. Over 90% of its production is derived from nitrogen and hydrogen via a catalytic process originally developed by Fritz Haber and Carl Bosch, utilizing an iron catalyst discovered by Alwin Mittasch [1]. For over a century, ammonia-based fertilizers have been essential to the global food supply. Currently, 85% of ammonia is used in fertilizer production, with 50% of global agriculture dependent on these fertilizers to enhance crop yields. The global ammonia market, valued at USD 53 billion in 2017, is projected to grow to USD 81 billion by 2025. While ammonia remains vital to agriculture due to well-established transportation and distribution systems, it is also being explored as a promising carbon-free energy carrier, boasting high hydrogen content (17.6 wt%), high energy density (4.25 kWh/L), and ease of storage and transport. [2].

The Haber-Bosch process is the most widely used method for producing ammonia and is one of the most important discoveries of the 20th century. It plays a critical role in manufacturing inorganic fertilizers, which are vital for feeding almost half of the global population [3]. However, the process has significant drawbacks, including high greenhouse gas emissions and substantial energy consumption, primarily due to the extreme operating pressures (100–200 atm) and temperatures (400–500 °C) required [4]. In light of these challenges, there is a growing demand for greener alternatives for ammonia production.

Various sustainable methods for ammonia synthesis have been developed, including the electrochemical Haber-Bosch process, electrochemical ammonia synthesis, and photocatalytic ammonia production. Electrochemical techniques are advantageous due to their milder operating conditions, ability to store renewable energy in chemical form, zero carbon dioxide emissions, and potential for localized ammonia production [2, 5]. However, it is worth noting that the performance of electrocatalysts toward NH_3 synthesis suffers from the poor Faradaic efficiencies mainly because of the competing hydrogen evolution reaction (HER), which has similar redox potentials, but faster reaction kinetics compared to the nitrogen reduction reaction (NRR). Recent advancements have been made by optimizing catalysts, reactors, and electrolytes to improve NH_3 synthesis performance. For example, using solid-state and molten salt electrolytes has led to high yield rates and current efficiencies for NH_3 production. Nevertheless, despite these improvements, electrochemical NRR still requires relatively high temperatures, which can increase NH_3 decomposition. Additionally, the complexity and cost of these electrolyzers add significant barriers to the commercialization of electrocatalytic NRR [6]. Other challenges remain for electrochemical nitrogen reduction reaction (NRR), such as the high bond dissociation energy of nitrogen, its high ionization potential and negative electron affinity, which added to its low

solubility in water impede both the thermodynamics and the kinetics of the reaction. As such, achieving high selectivity in electrochemical NRR continues to be a significant challenge [5].

Photocatalytic ammonia production, which harnesses light energy to convert nitrogen and water into ammonia, offers the advantage of utilizing renewable solar energy and was first reported by Schrauzer and Guth in 1977 [7]. In the referred work, ammonia was produced using a batch UV-illuminated reactor filled by N_2 gas and a humidified-TiO_2 (water-chemisorbed) powder. The authors also showed that the performance of the photocatalyst could be improved by adding an Fe dopant in the reaction. Recent advances in photocatalysts for ammonia synthesis have focused on exploring a variety of new materials. These materials include Fe_2O_3, ZnO, Ga_2O_3, and ZrO_2 due to their potential in facilitating photocatalytic reactions. Additionally, other classes of materials such as bismuth oxyhalides, carbon-based materials, metal sulfides, and biomimetic photocatalysts have been investigated for their promising photoreduction properties. Despite these advancements, key challenges remain in efficiently adsorbing and activating nitrogen molecules to drive the reaction effectively [8].

Among these materials, iron oxide has attracted significant attention due to its unique properties and potential to overcome existing challenges. Iron oxide nanoparticles are becoming increasingly significant for the advancement of innovative solutions in nanotechnology. Iron oxide has been widely studied in a wide range of applications, such as pigments, biomedical materials, electromagnetic devices, catalysis [9], N_2 photoreduction and photocatalysts. Khader et al. [10] reported that the production of ammonia using a catalyst made of a mixture of iron oxides. The catalyst mixture was prepared via a complicated high-temperature, partial-reduction procedure in a humid H_2 atmosphere. Iron plays a crucial role in ammonia synthesis due to several factors: it is abundant in the Earth's crust [11], interacts effectively with N_2 molecules [12] and absorbs H atoms [13]. Additionally, iron oxide (Fe_2O_3) is a narrow-bandgap semiconductor, making it a promising candidate for photocatalysis [14]. For these reasons, we have chosen to explore iron oxide as a solar energy material for the artificial photosynthesis of ammonia: its efficiency, non-toxicity, and low cost at ambient conditions make it an attractive option for further investigation in this field.

To further investigate the potential of the iron oxides, this manuscript reports on the efficacy of three technologically relevant iron oxide polymorphs, goethite (α-FeO(OH)), magnetite (Fe_3O_4) and hematite (α-Fe_2O_3), on the photocatalytic synthesis of ammonia from N_2 and water in ambient pressure and temperature. Our key motivation is to identify the most effective polymorph to serve as a basis for future surface and bandgap engineering.

2. EXPERIMENTAL SECTION

2.1 CATALYST PREPARATION

Hematite. The hematite nanopowders were synthesized by the polymeric precursor method[15]. It was used 45.8 wt% anhydride citric acid (Synth, $C_6H_8O_7$, ≥ 99.00 wt% purity), 30.5 wt% ethylene glycol (Synth, $C_2H_6O_2$, ≥ 99.00 wt% purity), and 23.6 wt% hydrated iron nitrate (Synth, $Fe(NO_3)_3$, ≥ 99.98 wt% purity), which was used as iron source. The calcination was carried out under air flow at 300 °C for 10 h in a muffle furnace.

Magnetite. Magnetite was prepared by a hydrothermal method [16] 5 mmol of $FeCl_3.6H_2O$ and 10 mmol of trisodium citrate were solubilized in 30 mL of deionized water under continuous stirring. The pH of the solution was adjusted to 7 using sodium hydroxide (NaOH). Finally, the colloidal suspension is transferred to an autoclave and maintained at 180 ºC for 24 hours. After cooling, the solid products are collected and washed three times with water, ethanol and water before being dried at 90 ºC.

Goethite. Goethite nanoparticles were also prepared using a hydrothermal method [17]. 8.25 mmol of $FeCl_3.6H_2O$ are dissolved in 30 mL of deionized water, to which 9.75 mmol of thiourea and 11.25 mmol of ethylenediamine are incorporated. The solution is transferred to an autoclave, sealed, and maintained at 120 ºC for 6 hours. After cooling naturally to ambient temperature, the solids are washed thoroughly with deionized water and ethanol and dried under vacuum for 5 h at 60 ºC.

2.2 CATALYST CHARACTERIZATION

Crystalline structure. Crystallographic information on the synthesized materials were obtained by powder X-ray Diffractometry (XRD) using an XRD-7000 (Shimadzu Inc.) diffractometer with Cu Kα radiation, operated at 45 kV and 35 mA. The step size was set at 0.05° 2θ per second over the 20-80° 2θ range. The data were processed in the software HighScore Plus for phase identification and quantification through the Rietveld method. An internal standard of magnesium aluminate was used in the refinement.

Microstructure. The microstructure of the catalysts was inspected using a scanning electron microscope with field emission gun (SEM-FEG) in an Inspect F50 (FEI Co.). Qualitative evaluation of the composition was carried out using the coupled electron-dispersion spectroscopy module (EDAX). Average agglomerate sizes and dimensions were evaluated by visual inspection using the software ImageJ (1.54g, NIH, USA).

Surface properties. The specific surface areas were determined by nitrogen gas adsorption at 77 K (Micromeritics Gemini VII 2390), according to the Brunauer-Emmett-Teller (BET) method. The samples were degassed at 90 °C for ~12 h before the experiment using a VacPrep 061 (Micromeritics Inc.). The surface states were inspected using infrared diffuse reflectance spectroscopy (DRIFTS) in a Nicolet iS50 FTIR spectrometer (Thermo Fisher Scientific Inc.). The analyses were carried out at 20 ºC under nitrogen atmosphere in an appropriate chamber (DiffusIR, Pike Technologies). The presence of acid sites was evaluated by the temperature-programmed desorption of NH_3 in a chemisorption analyzer (AutoChem II, Micromeritics Inc.). The samples were pretreated at 90 ºC under He flow for 1h, then cooled to 50 ºC prior to ammonia injection. Ammonia was injected at 50 ºC for 1h, after which He was flowed for 30 minutes at the same temperature. TPD data were collected upon heating the samples from 50 ºC to 700 ºC at a rate of 10 ºC/min under He flow. Thermogravimetric analyses (TGA) and differential scanning calorimetry (DSC) assays were carried out to identify specific thermal events such as dehydration, decomposition, and phase transitions within the materials over the temperature range of the TPD analyses. The analyses were performed using a STA 449 F3 Jupiter (Netzsch Analyzing & Testing) instrument, from 50 ºC to 800 ºC at a ramp of 10 ºC/min under N_2 flow. The samples were placed in open alumina crucibles to ensure uniform heat distribution and accurate thermal measurements.

Optoelectric properties. UV-Vis diffuse reflectance spectroscopy (Cary 5000, Varian) was used to estimate the bandgap energies of the prepared photocatalysts using the Tauc method [18]. The diffuse reflectance (R) spectra were converted to the Kubelka-Munk remission function $F(R) = (1-R)^2/2R$. Physical deactivation profiles were inspected by steady-state photoluminescence analysis using a fluorimeter (FL3-P, Horiba Co.). The analyses were carried out in an aqueous dispersion simulating the experimental conditions of the ammonia synthesis experiments (500 mg L^{-1}, under N_2 saturation) for the three oxides, and in powder phase for hematite. The samples were excited using wavelengths of 280 nm and 365 nm. Time-resolved photoluminescence (TRPL) measurements were carried out in the same equipment using a 1MHz LED laser pulse of 369 nm (NanoLED-370), mapping the emission at 433 nm, previously identified as peak emission in steady-state measurements. Decay data were analyzed in Origin using a stretched exponential function to evaluate the carrier lifetime distribution. Chopped-light chronoamperometry was employed to evaluate the electrochemical properties of the materials, using 0.5 and 1.2 V potentials. For this analysis, suspensions of 1 mg mL^{-1} in 1-propanol were prepared and sonicated for 30 minutes. Subsequently, 400 µL of these suspensions were drop-cast onto an FTO substrate, in a 1.0 × 1.0 cm area defined by Kapton tape. A three-electrode setup was connected to a µAutolab III potentiostat/galvanostat, with the deposited catalysts serving as the working

electrode, Ag/AgCl as the reference electrode, and a Pt wire as the counter-electrode. An aqueous 0.5 mol L^{-1} Na_2SO_4 solution was used as the electrolyte. A solar simulator equipped with an A.M. 1.5G filter, providing 100 mW cm^{-2} intensity, was used as the light source. The light intensity was measured with a Newport model 842-PE power meter and a light intensity detector (818-P-001-12).

2.3 PHOTOCATALYTIC ACTIVITY TEST

Photocatalytic tests were conducted using a system consisting of an annular photoreactor and a mixing tank, as illustrated in Figure 1. The photoreactor has an inner volume of 18 mL, comprising an outer PVC cylinder with two inlet/outlet ports prototyped in ABS designed to provide a helicoidal flow, and an inner quartz tube to provide a UVC-transparent irradiation window. In a typical experiment, 50 mg of the catalyst was dispersed in 250 mL of deionized water under continuous mechanical stirring. To ensure the removal of dissolved oxygen and achieve nitrogen saturation (approximately 17 mg L^{-1}), pure (99.999%) nitrogen gas (White Martins Gases Industriais LTDA) was bubbled through the solution for 20 minutes. The fluid was then recirculated between the reactor and the mixing tank for an additional 20 minutes, allowing the dispersed catalyst to be fully transferred into the annular photoreactor. Following this preparation period, the light source, a UVC tubular lamp (HNS 4W, Osram Inc.) placed coaxially inside the photoreactor, was switched on, and samples were collected every 60 minutes for 180 minutes while maintaining continuous recirculation, mixing, and N_2 bubbling.

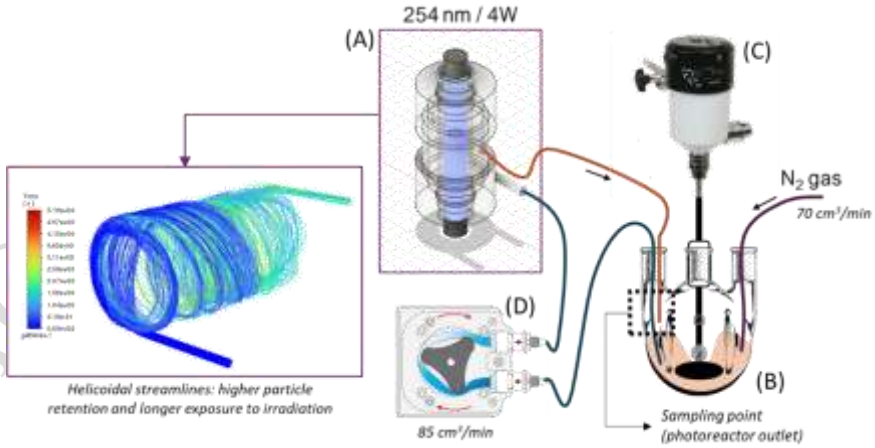

Figure 1. Illustration of the experimental setup comprising an annular photoreactor with tangential flow connections (A), a mixing tank with continuous N_2 gas feed (B) and a mechanical mixer with glass impeller (C), and a recirculating pump (D).

The formation of ammonia was quantified using the Berthelot reaction with a commercial ammonia test kit (LabconTest, Alcon LTDA). For each measurement, samples collected at the photoreactor outlet were filtered using a 0.22 µm PES filter (Kasvi), and 1.0 mL of the filtered

aliquot was mixed with 80 µL each of Solution 1 (an aqueous solution of phenol, sodium nitroprussiate and isopropanol), and Solution 2 (an aqueous solution of sodium hydroxide and sodium hypochlorite), producing a yellow-green solution. This solution was then transferred to a cuvette and analyzed using a spectrophotometer (IL-593-BI, Kasuaki) after 5 minutes. The progress of the reaction was monitored by measuring the absorbance at 680 nm, with quantification carried out using a previously prepared calibration curve. Blank tests were conducted by repeating the analytical procedure with Fe^{II}/Fe^{III} solutions, both with and without added ammonia, in place of the samples, to assess any potential interference with the spectroscopic measurements; no interference was observed.

3. RESULTS

3.1 CATALYST CHARACTERIZATION

The X-ray diffraction patterns for the synthesized iron oxide samples, shown in Figure 2A, confirm the success of the syntheses. The broad peaks observed are typical of nanosized crystallites.

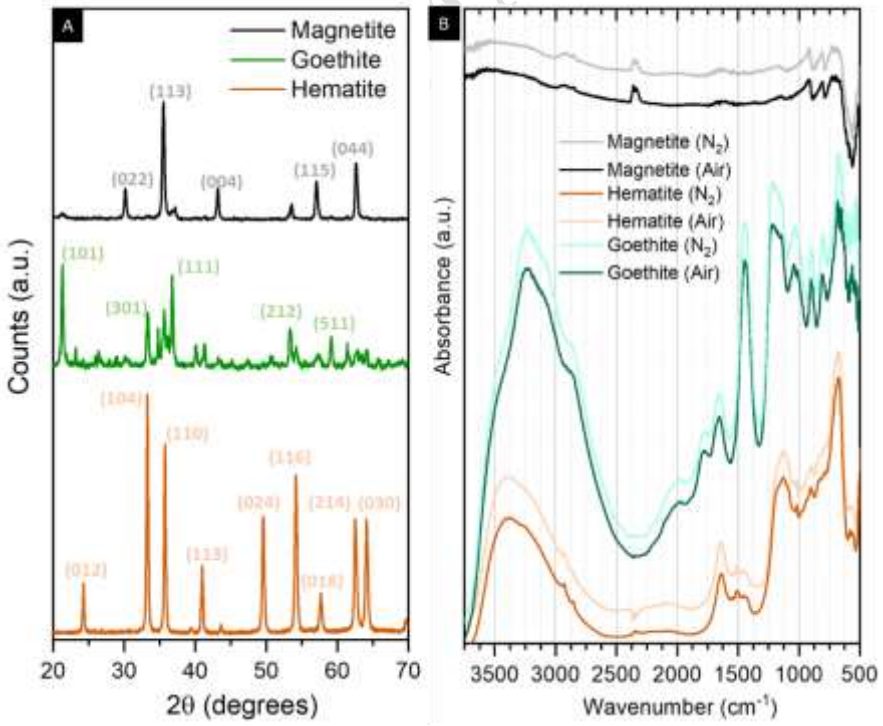

Figure 2. Microstructural and surface characterization of the synthesized materials. (A) XRD patterns with identification of the prevailing faces, (B), (C) and (D) SEM images of magnetite, goethite and hematite, respectively; (B) DRIFTS spectra of the three oxides in different atmospheres.

Peak identification and Rietveld refinement were performed using the crystallographic standards COD 96-900-5813 (Magnetite), COD 96-900-2160 (Goethite) and COD 96-901-5066 (Hematite). The refinements revealed that (i) the obtained crystallites are nanosized in nature with average diameters in the range of 30-40 nm, and (ii) that secondary phases were present in all materials, especially goethite. The crystallite sizes and phase compositions are summarized in Table 1, with the specific surface area quantified using the BET method.

Table 1. Selected properties of the synthesized materials.

Sample	Specific surface area (m^2/g)	Composition	Crystallite size (nm)
Magnetite	26.31 ± 0.08	90.4% Magnetite 9.6% Goethite	32.4 (M)
Goethite	27.20 ± 0.08	70% Goethite 21.6% Magnetite 8.4% Hematite	32.8 (G)
Hematite	14.00 ± 0.07	99.5% Hematite 0.5% Maghemite	39.4 (H)

The infrared spectra shown in Figure 2B also confirm the nature of the oxides and show their relative stability by the absence of significant changes in different atmospheres. The particularly wide bands of water and surface-bound -OH groups are noteworthy in the samples of hematite and goethite, confirming their highly hydrophilic character. The characteristic Fe-O-H bands [19] around 600-900 cm^{-1} typical of goethite are also clearly present in their spectra, and do not show any distinct changes in a drier atmosphere (N_2), suggesting the strong character of these groups.

A visual inspection of the microstructure of the oxides, shown in Figure 3, indicates that magnetite (Fig. 3A) forms spherical aggregates with an average diameter of 49 ± 13 μm (n = 18). A closer inspection shows that these aggregates are formed by octahedral particles of average length of 156 ± 26 nm (n = 37). Hematite particles (Fig. 3B), on the other hand, form platelet-like laminar structures with a characteristic diameter of 70 ± 24 nm (n = 24). Finally, goethite crystals (Fig. 3C) appear as agglomerates of irregular, flake-like layered structures with an average length of 28 ± 7 nm (n = 22). The highly porous structure observed in magnetite and goethite are reflected in their larger specific surface areas (Table 1), of ca. 26 $m^2\ g^{-1}$, while hematite showed a smaller area of ca. 14 $m^2\ g^{-1}$.

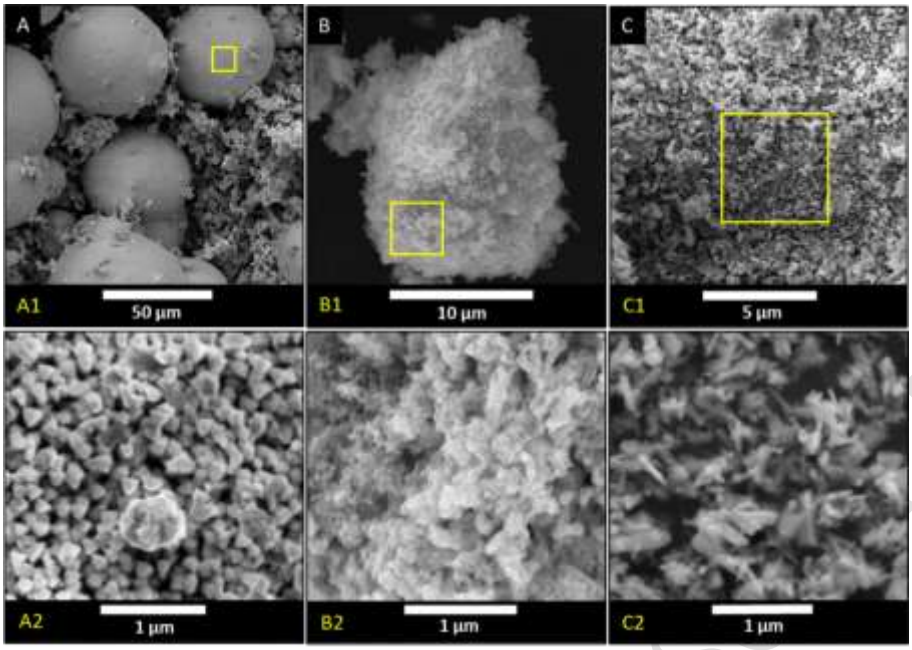

Figure 3. Micrographs of (A) magnetite, (B) hematite, and (C) goethite.

The thermal analysis of the three iron oxide samples is shown in Figure 4 for (A) magnetite, (B) goethite, and (C) hematite. The results reveal distinct behaviours in the NH_3-TPD, DTG, and DSC profiles. In the case of goethite, the TPD signal shows multiple desorption events, corresponding to pronounced endothermic peaks in the DSC curve, indicating the loss of structurally bound water and subsequent decomposition, with significant weight loss observed in the DTG. The mass loss endothermic band between 220-320 ºC can be ascribed to the dihydroxylation, i.e. the conversion of the hydroxide into oxide groups with the concomitant loss of water ($2OH^- \rightarrow O^{2-} + H_2O$) [20]. The deep endothermic band around 600 ºC is likely a result of the conversion of iron sulfates, formed from thiourea in the hydrothermal step, into hematite [21]. On the other hand, magnetite displays notable TPD peaks, suggesting the release of adsorbed or chemically bound species, alongside a significant endothermic DSC event around 300°C, indicating a phase transformation, which corresponds to a sharp mass loss in the DTG profile. Finally, hematite exhibits a relatively stable TPD signal with minimal desorption activity, consistent with its known thermal stability, and a nearly constant DSC profile, indicating minimal heat flow changes, while the DTG shows a gradual, steady mass loss, likely due to minor surface or impurity transformations, possibly residual carbon from the Pechini synthesis. Due to the decomposition of the samples, it was not possible to extract relevant information on the presence or strength of acid sites in the oxides.

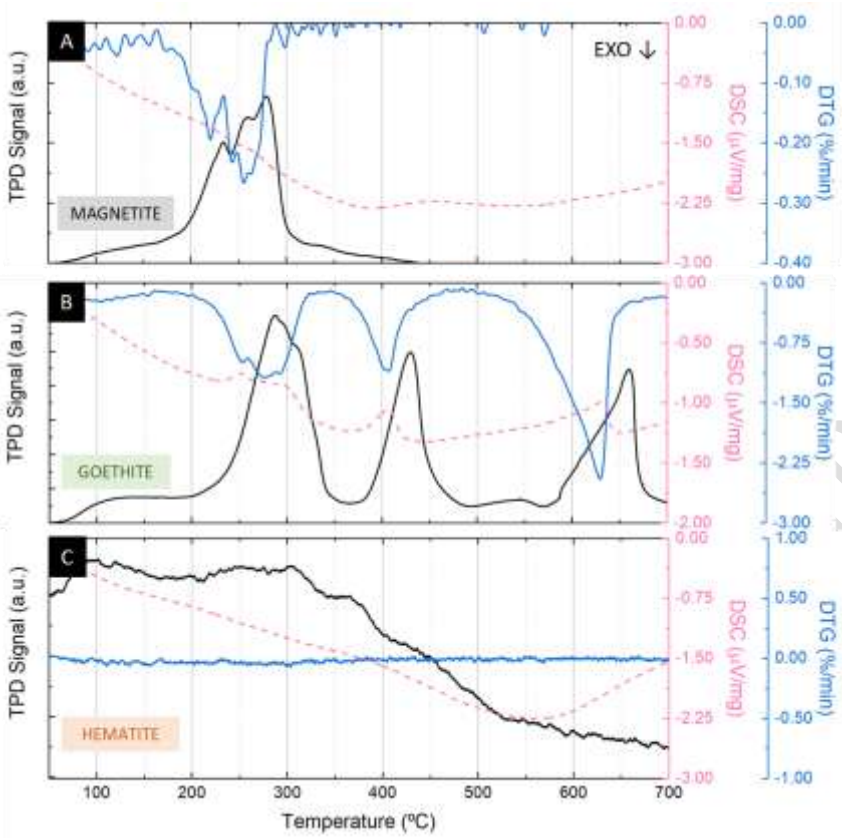

Figure 4. Thermal analyses (DTG, DSC and NH3-TPD) of (A) magnetite, (B) goethite and (C) hematite.

The optical properties of the oxides were analyzed using Tauc plots, shown in Figure 5. The plots were constructed to determine the optical bandgaps of direct (solid black lines) and indirect (dashed pink lines) allowed transitions. For goethite, the direct bandgap was determined to be 2.15 eV, while the indirect bandgap was slightly lower at 2.05 eV. These results corroborate the data reported by Liu et al. (2011) [22] where direct and indirect transition bandgaps of 2.15 eV and 2.06 eV were reported. Hematite exhibited similar behavior, with both distinct direct (2.02 eV) and indirect (2.09 eV) transitions, in line with previous calculations, such that of [23] who reported an indirect bandgap of 2.05 eV. In contrast, magnetite showed coincident values for both direct and indirect transitions, with a bandgap energy of 1.75 eV. This corresponds to the value found by Saragi et al. (2016) for a nanoparticles obtained by co-precipitation at 25°C [24]. DFT studies [25] how that magnetite's main transition is direct, with allowed bandgap energies of 1.94 eV or 1.47 eV, depending on the spin of the transitioning electron. The bandgap energies obtained from the Tauc plots indicate that all three iron oxide minerals exhibit semiconducting properties, with bandgap energies corresponding to approx. 700 nm for magnetite, 575 nm for goethite, and 600 nm for hematite.

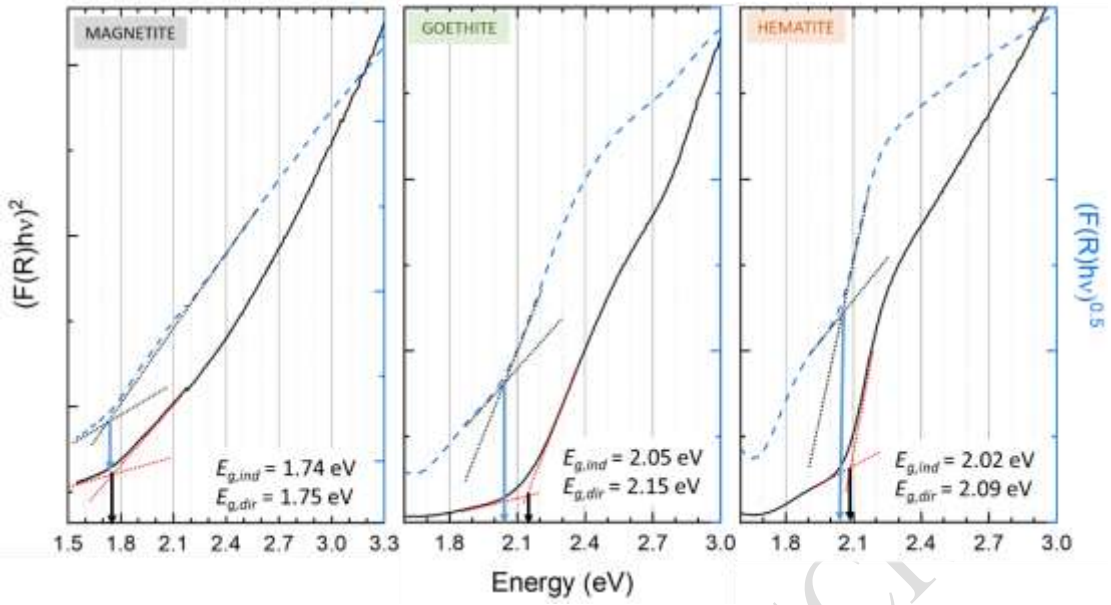

Figure 5. Tauc plots indicating the estimated direct (black solid lines) and indirect (dashed blue lines) bandgap energies of magnetite, goethite, and hematite.

3.2 PHOTOCATALYTIC PERFORMANCE

Table 2 summarizes the results of the photocatalytic tests. Goethite exhibited the best overall performance, achieving a specific rate of 20.6 μmol g^{-1} h^{-1}, as quantified after 180 min of irradiation after the accumulation of ammonia in the reaction system. Magnetite also demonstrated significant photoactivity; however, when surface area is taken into account, hematite actually outperformed both magnetite and goethite. The surface-specific rate is a more intrinsic measure of a material's catalytic capacity, as surface area is closely connected to the number of viable active sites. Therefore, the results suggest that despite its lower specific rate, hematite's activity could be significantly improved by adopting a synthesis procedure that yields a larger specific surface area. Since magnetite is not known for being photoactive, its photocatalytic performance is likely due to its mixed-phase structure containing 30% of the photoactive goethite phase, as shown in Table 1.

Table 2. Photocatalytic formation of ammonia using the three iron oxide species.

Material	Yield at 180 min (μg NH_4^+)	Specific rate (μmol NH_3 g^{-1} h^{-1})	Surface-specific rate (μmol NH_3 m^{-2} h^{-1})
Magnetite	29.66	10.34	0.39
Goethite	46.67	20.62	0.76
Hematite	23.11	8.55	1.05

Nevertheless, to interpret these observations, optoelectrical measurements were carried out, and the results are shown in Figure 6. The photoelectrochemical performance of the materials was evaluated under UV-Vis (solar simulator) and visible light (λ > 420 nm, solar simulator with UV

filter) irradiation, as depicted in Figures 6A and 6B. At 1.2 V, magnetite exhibited no response to either irradiation source, whereas goethite demonstrated a strong response to UV-Vis light but a weak response to visible light. In contrast, hematite produced the highest photocurrent under both visible and UV-Vis irradiation. A similar trend was observed at 0.5 V, with hematite showing greater stability at this lower potential. These results align with the findings of Baldovi et al. [26], who noted that hematite electrodes performed better under solar AM 1.5 G illumination than under visible light alone. Additionally, Xu et al. [27] reported a maximum stable photocurrent density of 1.96 mA cm^{-2} for hematite, which is consistent with our observations.

Photoluminescence measurements were carried out in powdered hematite (the most stable material) to understand the patterns of the electronic transitions following excitation, shown in Figure 6C. The powdered phase PL revealed three deactivation transitions with energies at 2.69, 2.88 and 3.02 eV (R^2 = 0.99867), similar to what was reported in the literature for nano-scale hematite [28]. These transitions can be associated with recombination events of the photogenerated electron-hole pairs from different electronic states of the material. The transition at 2.69 eV is particularly close to the crystal-field splitting energy of Fe^{3+} in an octahedral environment [29], suggesting that this transition corresponds to an electronic transition within the Fe^{3+} 3d orbitals in octahedrical sites of the hematite structure. This transition is prevalent, as shown in Figure 6D, when the material is excited in the UV-A range (365 nm). However, when the material is excited in the UV-C range (280 nm), the prevailing transition occurs at 2.88 eV, likely resulting from hybridized Fe 3d and O 2p states that are characteristic of CB minimum and VB maximum in hematite.

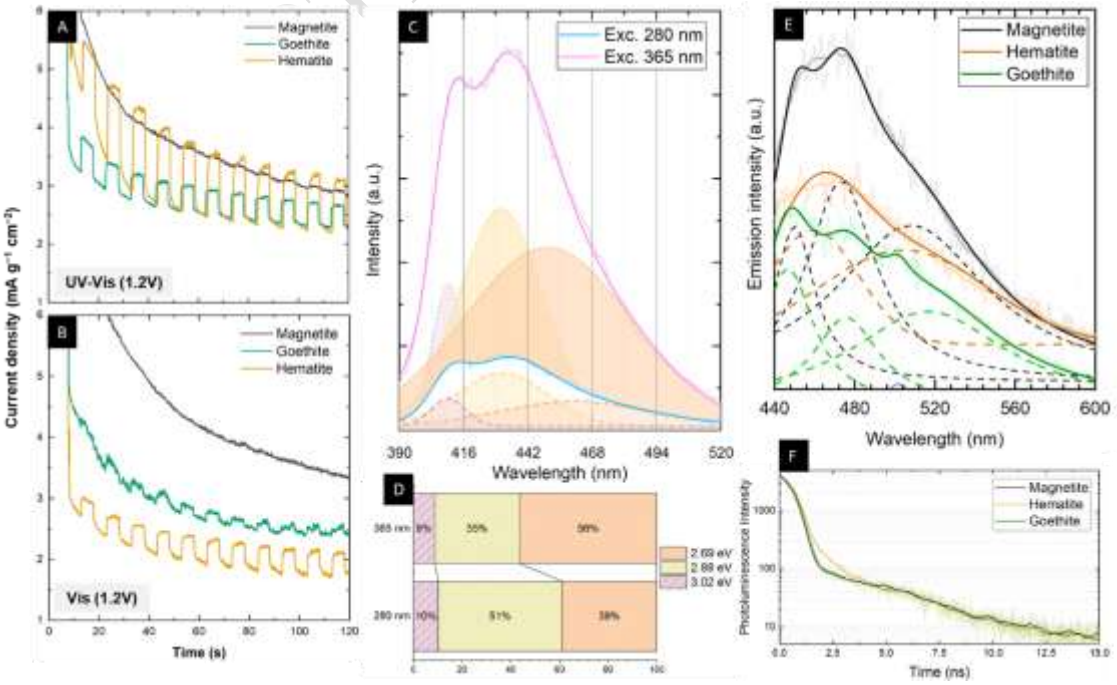

Figure 6. Photoelectrochemical properties of the iron oxides. (A) Photocurrent measurements of the three oxides in UV-Vis (300-800 nm) and (B) in Vis (420-800 nm) light with 1.2V of external bias. (C) Photoluminescence spectra and (D) distribution of emission energies of dry (powder) hematite obtained using 280 nm and 365 nm excitation wavelengths; (E) PL spectra of the three oxides in dispersed (aqueous) phase (excitation wavelength of 365 nm); and (F) TRPL spectra of the three oxides in aqueous solution (excitation wavelength of 365 nm).

In-situ PL measurements with the three oxides, shown in Figure 6E, revealed the occurrence of different electronic transitions in the three materials. The emissions of magnetite in situ show three transitions at 450.0 ± 0.8, 473.3 ± 1.4, and 508.3 ± 6.1 nm (2.76, 2.62, and 2.44 eV, R^2 = 0.9857), similar to the transitions observed for goethite, at 446.7 ± 0.4, 475.6 ± 0.9 and 516 ± 6.8 (R^2 = 0.9928). Hematite, on the other hand, showed only two transitions (R^2 = 0.9676), at 459.5 ± 0.8 and 504.2 ± 13.8 nm (2.70 and 2.46 eV). Considering the uncertainty of the fitting, it is likely that the transition around 500-516 represents the same recombination event, suggesting a common recombination pathway, likely influenced by surface states or defects prevalent in aqueous environments. Indeed, goethite exhibited the lowest PL signal, possibly because surface hydroxyl groups inhibit the recombination of photogenerated charging by acting as trapping states [30]. The paper by Huang et al. (2012) [31] provides critical insights into how the electronic environment and the presence of water can alter the dynamics of photogenerated carriers in hematite. Their transient absorption (TA) studies showed that under water oxidation conditions, photogenerated holes exhibit long-lived absorption features that are influenced by the surrounding environment. Specifically, they observed that the photogenerated holes have absorption bands at ~570 nm, which are attributed to transitions involving surface states and defects that are stabilized in an aqueous environment. In our case, the dispersion of the oxides in water likely leads to increased interaction between their surface and water molecules, resulting in the formation of hydroxyl groups or other surface modifications, which in turn introduce new defect states or stabilize existing ones. These states are likely responsible for the observed redshift in the PL emissions, as the recombination of electron-hole pairs now occurs from these defect states, leading to lower energy emissions compared to the dry powder. Klahr et al. [32] also emphasize the importance of surface chemistry, particularly hydroxylation, in determining the electronic properties of hematite and its likelihood to promote redox reactions.

Time-resolved photoluminescence (TRPL) measurements, illustrated in Figure 6F, further emphasize the distinct charge carrier dynamics among hematite, goethite, and magnetite. The data were fit using a stretched exponential function. Hematite exhibited an average lifetime τ = 0.83 ns, goethite showed a slightly shorter lifetime (τ = 0.78 ns), while magnetite presented the shortest lifetime (τ = 0.73 ns). These findings correlate with the lower photoluminescence (PL) intensity in goethite, suggesting that the surface hydroxyl groups suppress charge recombination by acting

as trapping states, as discussed in prior studies [30, 31]. The results converse with average charge-carrier lifetimes found in large bandgap semiconductors, such as TiO_2, reaching up to 1.17 ns due to effects of surface-adsorbed species [33] and agree with observations that iron oxides have typically faster recombination rates than common photocatalysts [34].

.

4. DISCUSSION

The formation of ammonia using the iron oxides is expected to proceed through a set of semi-reactions [7] with a high free energy change (ΔG (298K) = 339 kJ mol^{-1}), making it very unlikely to proceed spontaneously and hence justifying the use of an electrochemical or photochemical alternative. Figure 6 summarizes some of the most recently published materials in the literature for NH_3 production from the photoreduction of N_2 using liquid water as proton source [35-67]. In our experiments, we found that goethite displayed the highest specific rate, followed by magnetite and hematite, ranging from 8.5 to 20.6 μmol g^{-1} h^{-1}. The highest reported rate was achieved using a composite of hematite and graphitic carbon nitride (4380 μmol g^{-1} h^{-1}) [60]; and the lowest, using Cr-doped TiO_2 (0.37 μmol g^{-1} h^{-1}) [35]. Figure 7A shows a box plot of the distribution of the specific ammonia production rates. After excluding the outliers of the distribution, the average reported yield was found to be 100.2 μmol g^{-1} h^{-1}, while the median is around 78.9 μmol g^{-1} h^{-1}. A detailed hierarchical clustering heatmap is shown in Figure 7B, with the materials reported in this work highlighted in a red box. The figure shows that the rates achieved by the iron oxides are aligned with the observed results of photocatalysts working under UV irradiation without scavengers (i.e. sacrificial reagents that extend the electron-hole pair lifetime). The fastest specific rate in the dataset obtained after exclusion of the outliers was reported for an Fe-doped TiO_2 (400 μmol g^{-1} h^{-1}) using a UV light source and ethanol as scavenger. A comparison with other TiO_2-based materials reveals the importance of the scavenger in accelerating the formation of ammonia, although its use brings about new chemical species into the system, increasing the complexity of a downstream separation process.

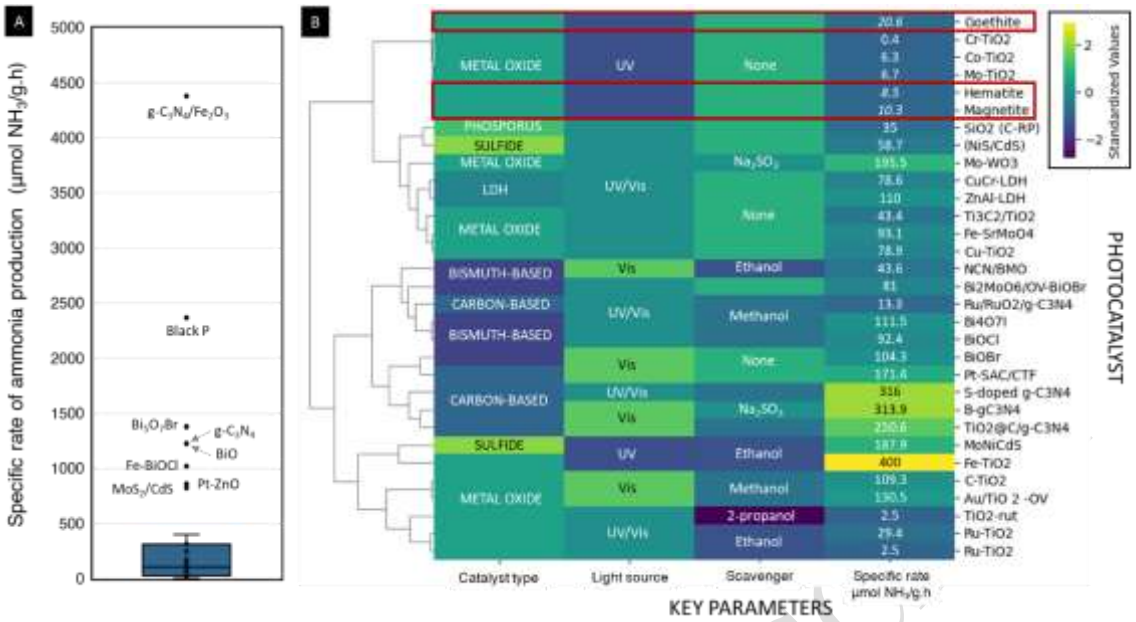

Figure 7. Material performance for the photoreduction of N_2 in liquid water. (A) Distribution of reported specific rates of ammonia production; and (B) heatmap detailing the observed rates as function of the scavenger used, the light source, and the catalyst material.

In our experiments, we found that goethite displayed the highest ammonia production rates among the iron oxides. This can be understood from their microstructure, showing a high density of agglomerates with an apparent high porosity, which could explain the observed higher surface areas and higher mass-based activities exhibited. Another relevant aspect is the stability of surface hydroxyl groups, which can play a significant role in the formation of protons in the vicinity of adsorbed nitrogen and, hence, contribute to the formation of ammonia. The works by Tennakone [68, 69] emphasized the critical role of hydration in iron oxides for effective nitrogen fixation. The stability and high photocatalytic activity of goethite under UV irradiation align with the observations of Tennakone's hydrous ferric oxide system, suggesting that the hydrated surface of goethite enhances nitrogen adsorption and activation, leading to more efficient ammonia synthesis. The prevalence of these structures may counterbalance the apparently lower generation of carriers on goethite than hematite (0.4 mA g^{-1} cm^{-2} versus 1.1 mA g^{-1} cm^{-2} with 1.2V bias). A likely explanation resides in the much faster carrier mobility of hematite (~10^{-2} versus ~10^{-5} cm^2 V^{-1} s^{-1}) [70, 71], which may induce recombination events resulting in a less efficient charge-carrier pair consumption. Moreover, goethite's lower photoluminescence (PL) signal, which might seem contradictory given its high catalytic efficiency, can be attributed to the role of surface hydroxyl groups acting as trap states. By trapping the carriers, they reduce PL intensity while simultaneously introducing new electronic transitions at higher energies, as evidenced by the distinct PL spectrum of goethite. Therefore, the lower PL emission in goethite possibly reflects more efficient electron/hole consumption at the surface, rather than an inherent inefficiency in

photocatalytic activity, which might explain its good photocatalytic performance, despite its PL emission and the lower generation of free carriers.

The light source used in the experiment has a monocromatic (254 nm) UV-C power (P_{em}) of 0.8 W. Since the reactor surrounds the lamp, it is safe to assume that all emitted photons enter the reaction volume. This hypothesis results in an average photon flow of 1.7 µmol photons s^{-1}. Thus, we can calculate the apparent quantum yield, *i.e.* the molar yield of ammonia per mol of photons irradiated in the reaction volume, $\Phi^{a}_{+NH_3}$ from the yields of ammonia reported in Table 1 (Y_{180}), following Equation 1:

$$\Phi^{a}_{+NH_3} = \frac{Y_{180}}{\phi_p t} = \frac{Y_{180}\,\lambda\,N_A}{P_{em}\,t\,hc} \quad (1)$$

where ϕ_p is the photon flow, amount based (µmol photons s^{-1}), t is the reaction time (10 800 s), N_A, h and c are the Avogadro number (photons mol^{-1}), the Planck constant (J s), and the speed of light in vacuum (m s^{-1}). Table 3 summarizes the results. The apparent quantum yields are substantially smaller than engineered systems, but are within the range of reported results, which vary from 0.013% for a MoO_3 photocatalyst [72] to as high as 13.6% for a mixed-phase TiO_2 (P25) modified with an alkali amine [73]. Apart from this clear outlier, the average apparent yield (median) for a variety of reported photocatalysts is 0.79% [74, 75].

Table 3. Apparent quantum yields of ammonia formation calculated for the iron oxides.

Material	Apparent quantum yield (%)
Magnetite	0.007
Goethite	0.017
Hematite	0.009

Considering the measured direct bandgaps (E_g) and the calculated electronegativity (χ) of the materials, we estimated the valence and conduction band edge energies (E_{VB} and E_{CB}) using Equations 2 and 3 [76-78] :

$$E_{VB} = \chi - E_e + \frac{1}{2}E_g \quad (2)$$

$$E_{CB} = E_{VB} - E_g \quad (3)$$

This allowed for the construction of the energy diagrams shown in Figure 8A.

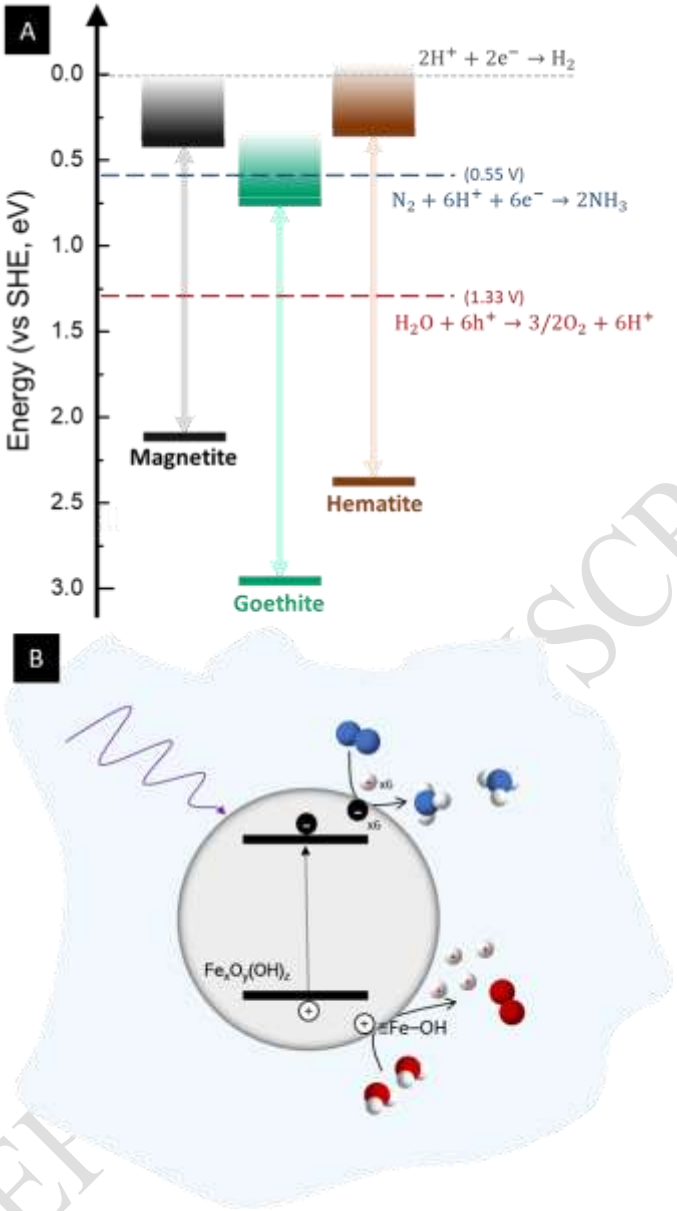

Figure 8. (A) Band energies of the three iron polymorphs reported in this manuscript, with the redox potentials of the key reactions involved in the photochemical N_2 reduction mechanism. (from [79]) (B) Schematic representation of the main reactions involved.

The band energies indicate that the energy required to reduce nitrogen is almost outside the range of the CB of the oxides, justifying the poor quantum yields observed in our work. As discussed before, the mechanism of N_2 reduction likely involves electron transfer reactions from and among surface-bound Fe^{II} and Fe^{III}, and the hydroxylated species, as similarly reported for other photochemical systems [30]. Upon N_2 adsorption, neighboring Fe-OH groups facilitate protonation and electron transfer to the nitrogen, forming reactive intermediates such as -NH and -NH_2, a process crucial for the stepwise reduction of N_2, which involves multiple proton-coupled electron transfers. Bulk conduction band electrons might not have sufficient energy to reduce N_2

directly, but the protonation steps promoted by the Fe-OH species might provide a more energetically favorable pathway, thus enabling the reduction reaction to proceed efficiently, which could explain the formation of ammonia even in FeOOH solutions, as discussed by Tennakone and colleagues [69].

5. CONCLUSION

This study provides a comparative analysis of three common iron oxide polymorphs – goethite, magnetite, and hematite – in the context of photocatalytic ammonia synthesis, highlighting goethite's promising performance due to its unique surface chemistry. Our results underscore the critical role of surface hydroxylation and specific morphological features in enhancing nitrogen reduction, suggesting that targeted approaches in surface and bandgap engineering could further improve catalytic efficiency. While the apparent quantum yields are low, the average specific ammonia production rates indicate the potential of these materials for continued optimization.

Goethite, despite its lower photocurrent and higher-energy conduction band edge, demonstrated superior performance; however, its limited thermal stability, with decomposition beginning at relatively low temperatures (~200 ºC), could restrict its long-term application, posing a challenge for future studies aiming to enhance its stability. Magnetite showed modest activity, with yields slightly higher than those of hematite, likely due to its mixed-phase structure (30% goethite) and highly organized microstructure. This suggests that creating heterojunctions with multiple iron oxide polymorphs could be a viable strategy to enhance ammonia production.

In contrast, hematite, the most stable iron oxide polymorph, exhibited high surface-specific reaction rates and a longer charge-carrier lifetime, placing it as a strong candidate for future bandgap and surface engineering improvements, echoing frequent comments in the literature [60]. Overall, our findings emphasize the importance of stability and morphology in the design of efficient photocatalysts for direct ammonia synthesis from N_2 gas in ambient temperature and pressures using water as a proton source.

ACKNOWLEDGEMENTS

The authors acknowledge the support of the São Paulo Research Foundation (FAPESP, Grant 23/14214-4). CAPA and PHP gratefully acknowledge the support of the Coordenação de Aperfeiçoamento de Pessoal de Nível Superior - Brasil (CAPES) - Finance Code 88887.672867/2022-00 and of the Human Resources Program of the National Agency for

Petroleum, Natural Gas and Biofuels – PRH-ANP, supported with resources from the investment of oil companies qualified in the Clause of P, D&I of Resolution ANP No. 50/2015 (PRH 49- UFABC), respectively. BR and BP express their gratitude for the institutional support from the Ignatian Educational Foundation (FEI) and thank the undergraduate students YS Casseb, RP de Oliveira, and PCP Gonçalves for their assistance during some experimental stages of this research.

The authors are also grateful for the technical support provided by Dr. EV de Oliveira, Dr. S. Carvalho, Mr. HL Piva, and Dr. YES Correales in the TPD, DSC, and PL analyses. The essential infrastructure support provided by the Research Center for Greenhouse Gas Innovation (RCGI), the Institute for Nuclear and Energy Research (IPEN/CNEN), and the University of São Paulo, through the Laboratory for Technological Characterization (LCT) and the Center for Nanotechnology and Tissue Engineering (CNET), is also acknowledged.

REFERENCES

[1] A. Mittasch and W. Frankenburg, "Early Studies of Multicomponent Catalysts," (Advances in Catalysis, 1950, pp. 81-104.

[2] M. Wang *et al.*, "Can sustainable ammonia synthesis pathways compete with fossil-fuel based Haber–Bosch processes?," *Energy & Environmental Science,* vol. 14, no. 5, pp. 2535-2548, 2021.

[3] V. Smil, "Detonator of the population explosion," *Nature,* vol. 400, p. 415, 1999.

[4] S. Zhang, Y. Zhao, R. Shi, G. I. N. Waterhouse, and T. Zhang, "Photocatalytic ammonia synthesis: Recent progress and future," *EnergyChem,* vol. 1, no. 2, 2019.

[5] T. Wu, W. Fan, Y. Zhang, and F. Zhang, "Electrochemical synthesis of ammonia: Progress and challenges," *Materials Today Physics,* vol. 16, 2021.

[6] R. Zhao *et al.*, "Recent progress in the electrochemical ammonia synthesis under ambient conditions," *EnergyChem,* vol. 1, no. 2, 2019.

[7] G. N. S. a. T. D. Guth, "Photolysis of water and photoreduction of Nitrogen on Titanium Dioxide," *Journal of the American Chemical Society,* pp. 7189-7193, 1977.

[8] K. Ithisuphalap, H. Zhang, L. Guo, Q. Yang, H. Yang, and G. Wu, "Photocatalysis and Photoelectrocatalysis Methods of Nitrogen Reduction for Sustainable Ammonia Synthesis," *Small Methods,* vol. 3, no. 6, 2018.

[9] S. A. C. Carabineiro, N. Bogdanchikova, P. B. Tavares, and J. L. Figueiredo, "Nanostructured iron oxide catalysts with gold for the oxidation of carbon monoxide," *RSC Advances,* vol. 2, no. 7, 2012.

[10] G. H. V. M.Khader, K.Kim, M.Salmerón and G.A.Somorjai, "Photoassisted Catalytic Dissociation of H2O To Produce Hydrogen on Partially Reduced α-Fe203," *J. Am. Chem. Society,* vol. 109, no. 12, pp. 3581–3585, 1987.

[11] M. Lashgari and P. Zeinalkhani, "Photocatalytic N 2 conversion to ammonia using efficient nanostructured solar-energy-materials in aqueous media: A novel hydrogenation

strategy and basic understanding of the phenomenon," *Applied Catalysis A: General,* vol. 529, pp. 91-97, 2017.

[12] C. J. H. Jacobsen, S. Dahl, B. G. S. Clausen, S. Bahn, A. Logadottir, and J. K. Nørskov, "Catalyst design by interpolation in the periodic table: Bimetallic ammonia synthesis catalysts [2]," *Journal of the American Chemical Society,* Letter vol. 123, no. 34, pp. 8404-8405, 2001.

[13] D. E. Jiang and E. A. Carter, "Diffusion of interstitial hydrogen into and through bcc Fe from first principles," *Physical Review B,* vol. 70, no. 6, 2004.

[14] H. Pan, X. Meng, and G. Qin, "Hydrogen generation by water splitting on hematite (0001) surfaces: First-principles calculations," *Physical Chemistry Chemical Physics,* Article vol. 16, no. 46, pp. 25442-25448, 2014.

[15] P. A. Lessing, "Mixed-cation oxide powders via polymeric precursors," *American Ceramic Society,* vol. 68, pp. 1002-1007, 1989.

[16] C. Han, D. Zhao, C. Deng, and K. Hu, "A facile hydrothermal synthesis of porous magnetite microspheres," *Materials Letters,* vol. 70, pp. 70-72, 2012.

[17] R. Zamiri, H. A. Ahangar, A. Zakaria, G. Zamiri, H. R. Bahari, and G. P. C. Drummen, "Hydrothermal synthesis of goethite (α-FeOOH) nanorods in the presence of ethylenediamine:thiourea," *Journal of Nanoparticle Research,* vol. 16, no. 4, 2014.

[18] P. Makula, M. Pacia, and W. Macyk, "How To Correctly Determine the Band Gap Energy of Modified Semiconductor Photocatalysts Based on UV-Vis Spectra," *J Phys Chem Lett,* vol. 9, no. 23, pp. 6814-6817, Dec 6 2018.

[19] H. Cui, W. Ren, P. Lin, and Y. Liu, "Structure control synthesis of iron oxide polymorph nanoparticles through an epoxide precipitation route," *Journal of Experimental Nanoscience,* vol. 8, no. 7-8, pp. 869-875, 2013/10/01 2013.

[20] "Characterization," in *The Iron Oxides*, 2003, pp. 139-183.

[21] P. P. M. Ribeiro, L. C. M. de Souza, R. Neumann, I. D. dos Santos, and A. J. B. Dutra, "Nickel and cobalt losses from laterite ore after the sulfation-roasting-leaching processing," *Journal of Materials Research and Technology,* vol. 9, no. 6, pp. 12404-12415, 2020.

[22] G. Liu, S. Liao, D. Zhu, L. Liu, D. Cheng, and H. Zhou, "Photodegradation of aniline by goethite doped with boron under ultraviolet and visible light irradiation," *Materials Research Bulletin,* vol. 46, no. 8, pp. 1290-1295, 2011.

[23] C. Xia, Y. Jia, M. Tao, and Q. Zhang, "Tuning the band gap of hematite α-Fe2O3 by sulfur doping," *Physics Letters A,* vol. 377, no. 31-33, pp. 1943-1947, 2013.

[24] T. Saragi, B. L. Depi, S. Butarbutar, B. Permana, and Risdiana, "The impact of synthesis temperature on magnetite nanoparticles size synthesized by co-precipitation method," *Journal of Physics: Conference Series,* vol. 1013, 2018.

[25] J. Noh, O. I. Osman, S. G. Aziz, P. Winget, and J. L. Bredas, "A density functional theory investigation of the electronic structure and spin moments of magnetite," *Sci Technol Adv Mater,* vol. 15, no. 4, p. 044202, Aug 2014.

[26] H. G. Baldovi, "Optimization of alpha-Fe(2)O(3) Nanopillars Diameters for Photoelectrochemical Enhancement of alpha-Fe(2)O(3)-TiO(2) Heterojunction," *Nanomaterials (Basel),* vol. 11, no. 8, Aug 7 2021.

[27] Y. Xu, H. Zhang, D. Gong, Y. Chen, S. Xu, and P. Qiu, "Solar water splitting with nanostructured hematite: the role of oxygen vacancy," *Journal of Materials Science,* vol. 57, no. 42, pp. 19716-19729, 2022.

[28] L. E. Mathevula, L. L. Noto, B. M. Mothudi, and M. S. Dhlamini, "Structural and optical properties of α-Fe2O3 nanoparticles, influence by holmium ions," *Physica B: Condensed Matter,* vol. 535, pp. 258-261, 2018/04/15/ 2018.

[29] C. Lohaus, C. Steinert, J. Brötz, A. Klein, and W. Jaegermann, "Systematic Investigation of the Electronic Structure of Hematite Thin Films," *Advanced Materials Interfaces,* vol. 4, no. 20, p. 1700542, 2017/10/01 2017.

[30] Z. Ma and H. Cheng, "Insights into the Photochemical Mechanism of Goethite: Roles of Different Types of Surface Hydroxyl Groups in Reactive Oxygen Species Generation and Fe(III) Reduction," *Environ Sci Technol,* vol. 58, no. 33, pp. 14812-14822, Aug 20 2024.

[31] Z. Huang *et al.*, "In situ probe of photocarrier dynamics in water-splitting hematite (α-Fe2O3) electrodes," *Energy & Environmental Science,* 10.1039/C2EE22681B vol. 5, no. 10, pp. 8923-8926, 2012.

[32] B. Klahr, S. Gimenez, F. Fabregat-Santiago, T. Hamann, and J. Bisquert, "Water Oxidation at Hematite Photoelectrodes: The Role of Surface States," *Journal of the American Chemical Society,* vol. 134, no. 9, pp. 4294-4302, 2012/03/07 2012.

[33] R. Brüninghoff, K. Wenderich, J. P. Korterik, B. T. Mei, G. Mul, and A. Huijser, "Time-Dependent Photoluminescence of Nanostructured Anatase TiO2 and the Role of Bulk and Surface Processes," *The Journal of Physical Chemistry C,* vol. 123, no. 43, pp. 26653-26661, 2019.

[34] H. Li, M. Guo, Z. Zhou, R. Long, and W. H. Fang, "Excitation-Wavelength-Dependent Charge-Carrier Lifetime in Hematite: An Insight from Nonadiabatic Molecular Dynamics," *J Phys Chem Lett,* vol. 14, no. 10, pp. 2448-2454, Mar 16 2023.

[35] G. N. Schrauzer and T. J. J. o. t. A. C. S. Guth, "Photolysis of water and photoreduction of nitrogen on titanium dioxide," 1977.

[36] L. Lin, Q. Zhu, A. Cheng, and L. Ma, "Efficient solar-driven nitrogen fixation over an elemental phosphorus photocatalyst," *Catalysis Science & Technology,* vol. 10, no. 12, pp. 4119-4125, 2020.

[37] X. Gao *et al.*, "Enhanced photocatalytic N(2) fixation by promoting N(2) adsorption with a co-catalyst," *Sci Bull (Beijing),* vol. 64, no. 13, pp. 918-925, Jul 15 2019.

[38] N. Zhang *et al.*, "Refining Defect States in W(18)O(49) by Mo Doping: A Strategy for Tuning N(2) Activation towards Solar-Driven Nitrogen Fixation," *J Am Chem Soc,* vol. 140, no. 30, pp. 9434-9443, Aug 1 2018.

[39] Y. Zhao *et al.*, "Layered Double Hydroxide Nanostructured Photocatalysts for Renewable Energy Production," *Advanced Energy Materials,* vol. 6, no. 6, 2015.

[40] S. Zhang *et al.*, "Sub-3 nm Ultrafine Cu(2) O for Visible Light Driven Nitrogen Fixation," *Angew Chem Int Ed Engl,* vol. 60, no. 5, pp. 2554-2560, Feb 1 2021.

[41] Y. Liao *et al.*, "2D-layered Ti3C2 MXenes for promoted synthesis of NH3 on P25 photocatalysts," *Applied Catalysis B: Environmental,* vol. 273, 2020.

[42] J. Luo *et al.*, "Band structure engineering of bioinspired Fe doped SrMoO4 for enhanced photocatalytic nitrogen reduction performance," *Nano Energy,* vol. 66, 2019.

[43] Y. Zhao *et al.*, "Tuning Oxygen Vacancies in Ultrathin TiO(2) Nanosheets to Boost Photocatalytic Nitrogen Fixation up to 700 nm," *Adv Mater,* vol. 31, no. 16, p. e1806482, Apr 2019.

[44] E. Vesali-Kermani, A. Habibi-Yangjeh, H. Diarmand-Khalilabad, and S. Ghosh, "Nitrogen photofixation ability of g-C(3)N(4) nanosheets/Bi(2)MoO(6) heterojunction photocatalyst under visible-light illumination," *J Colloid Interface Sci,* vol. 563, pp. 81-91, Mar 15 2020.

[45] X. Xue *et al.*, "Efficient photocatalytic nitrogen fixation under ambient conditions enabled by the heterojunctions of n-type Bi(2)MoO(6) and oxygen-vacancy-rich p-type BiOBr," *Nanoscale,* vol. 11, no. 21, pp. 10439-10445, May 30 2019.

[46] H. Wang, X. Li, Q. Ruan, and J. Tang, "Ru and RuO(x) decorated carbon nitride for efficient ammonia photosynthesis," *Nanoscale,* vol. 12, no. 23, pp. 12329-12335, Jun 21 2020.

[47] Y. Bai *et al.*, "Facet-Dependent Photocatalytic N(2) Fixation of Bismuth-Rich Bi(5)O(7)I Nanosheets," *ACS Appl Mater Interfaces,* vol. 8, no. 41, pp. 27661-27668, Oct 19 2016.

[48] H. Li, J. Shang, J. Shi, K. Zhao, and L. Zhang, "Facet-dependent solar ammonia synthesis of BiOCl nanosheets via a proton-assisted electron transfer pathway," *Nanoscale,* vol. 8, no. 4, pp. 1986-93, Jan 28 2016.

[49] H. Li, J. Shang, Z. Ai, and L. Zhang, "Efficient Visible Light Nitrogen Fixation with BiOBr Nanosheets of Oxygen Vacancies on the Exposed 001 Facets," *J Am Chem Soc,* vol. 137, no. 19, pp. 6393-9, May 20 2015.

[50] J. Li *et al.*, "Single-Atom Pt–N3 Sites on the Stable Covalent Triazine Framework Nanosheets for Photocatalytic N2 Fixation," *ACS Catalysis,* vol. 10, no. 4, pp. 2431-2442, 2020.

[51] S. Cao, B. Fan, Y. Feng, H. Chen, F. Jiang, and X. Wang, "Sulfur-doped g-C3N4 nanosheets with carbon vacancies: General synthesis and improved activity for simulated solar-light photocatalytic nitrogen fixation," *Chemical Engineering Journal,* vol. 353, pp. 147-156, 2018.

[52] W. Wang *et al.*, "Formation of B□N□C Coordination to Stabilize the Exposed Active Nitrogen Atoms in g-C(3) N(4) for Dramatically Enhanced Photocatalytic Ammonia Synthesis Performance," *Small,* vol. 16, no. 13, p. e1906880, Apr 2020.

[53] Q. Liu, L. Ai, and J. Jiang, "MXene-derived TiO2@C/g-C3N4 heterojunctions for highly efficient nitrogen photofixation," *Journal of Materials Chemistry A,* vol. 6, no. 9, pp. 4102-4110, 2018.

[54] Y. Cao *et al.*, "Photofixation of atmospheric nitrogen to ammonia with a novel ternary metal sulfide catalyst under visible light," *RSC Advances,* vol. 6, no. 55, pp. 49862-49867, 2016.

[55] W. Zhao *et al.*, "Enhanced nitrogen photofixation on Fe-doped TiO2 with highly exposed (101) facets in the presence of ethanol as scavenger," *Applied Catalysis B: Environmental,* vol. 144, pp. 468-477, 2014.

[56] J. Yang *et al.*, "High-Efficiency "Working-in-Tandem" Nitrogen Photofixation Achieved by Assembling Plasmonic Gold Nanocrystals on Ultrathin Titania Nanosheets," *J Am Chem Soc,* vol. 140, no. 27, pp. 8497-8508, Jul 11 2018.

[57] H. Hirakawa, M. Hashimoto, Y. Shiraishi, and T. Hirai, "Photocatalytic Conversion of Nitrogen to Ammonia with Water on Surface Oxygen Vacancies of Titanium Dioxide," *J Am Chem Soc,* vol. 139, no. 31, pp. 10929-10936, Aug 9 2017.

[58] K. T. Ranjit, T. K. Varadarajan, and B. Viswanathan, "Photocatalytic reduction of dinitrogen to ammonia over noble-metal-loaded TiO2," *Journal of Photochemistry and Photobiology A: Chemistry,* vol. 96, no. 1, pp. 181-185, 1996/05/31/ 1996.

[59] S. Liu *et al.*, "Photocatalytic Fixation of Nitrogen to Ammonia by Single Ru Atom Decorated TiO2 Nanosheets," *ACS Sustainable Chemistry & Engineering,* vol. 7, no. 7, pp. 6813-6820, 2019.

[60] H. Mou *et al.*, "A one-step deep eutectic solvent assisted synthesis of carbon nitride/metal oxide composites for photocatalytic nitrogen fixation," *Journal of Materials Chemistry A,* vol. 7, no. 10, pp. 5719-5725, 2019.

[61] S. Bian, M. Wen, J. Wang, N. Yang, P. K. Chu, and X. F. Yu, "Edge-Rich Black Phosphorus for Photocatalytic Nitrogen Fixation," *J Phys Chem Lett,* vol. 11, no. 3, pp. 1052-1058, Feb 6 2020.

[62] S. Wang *et al.*, "Light-Switchable Oxygen Vacancies in Ultrafine Bi(5) O(7) Br Nanotubes for Boosting Solar-Driven Nitrogen Fixation in Pure Water," *Adv Mater,* vol. 29, no. 31, Aug 2017.

[63] G. Dong, W. Ho, and C. Wang, "Selective photocatalytic N2 fixation dependent on g-C3N4 induced by nitrogen vacancies," *Journal of Materials Chemistry A,* vol. 3, no. 46, pp. 23435-23441, 2015.

[64] S. Sun, Q. An, W. Wang, L. Zhang, J. Liu, and W. A. Goddard Iii, "Efficient photocatalytic reduction of dinitrogen to ammonia on bismuth monoxide quantum dots," *Journal of Materials Chemistry A,* vol. 5, no. 1, pp. 201-209, 2017.

[65] N. Zhang, L. Li, Q. Shao, T. Zhu, X. Huang, and X. Xiao, "Fe-Doped BiOCl Nanosheets with Light-Switchable Oxygen Vacancies for Photocatalytic Nitrogen Fixation," *ACS Applied Energy Materials,* vol. 2, no. 12, pp. 8394-8398, 2019.

[66] C. M. Janet, S. Navaladian, B. Viswanathan, T. K. Varadarajan, and R. P. Viswanath, "Heterogeneous Wet Chemical Synthesis of Superlattice-Type Hierarchical ZnO Architectures for Concurrent H2 Production and N2 Reduction," *The Journal of Physical Chemistry C,* vol. 114, no. 6, pp. 2622-2632, 2010/02/18 2010.

[67] B. Sun, Z. Liang, Y. Qian, X. Xu, Y. Han, and J. Tian, "Sulfur Vacancy-Rich O-Doped 1T-MoS(2) Nanosheets for Exceptional Photocatalytic Nitrogen Fixation over CdS," *ACS Appl Mater Interfaces,* vol. 12, no. 6, pp. 7257-7269, Feb 12 2020.

[68] K. Tennakone, S. Wickramanayake, C. A. N. Fernando, O. A. Ileperuma, and S. Punchihewa, "Photocatalytic nitrogen reduction using visible light," *Journal of the Chemical Society, Chemical Communications,* 10.1039/C39870001078 no. 14, pp. 1078-1080, 1987.

[69] K. Tennakone *et al.*, "Photoreduction of dinitrogen to ammonia by ultrafine particles of iron hydroxide oxide (Fe(O)OH) formed by photohydrolysis of iron(II) bicarbonate," *Langmuir,* vol. 7, no. 10, pp. 2166-2168, 1991/10/01 1991.

[70] C. S. Ahart, K. M. Rosso, and J. Blumberger, "Electron and Hole Mobilities in Bulk Hematite from Spin-Constrained Density Functional Theory," *J Am Chem Soc,* vol. 144, no. 10, pp. 4623-4632, Mar 16 2022.

[71] V. Alexandrov and K. M. Rosso, "Electron transport in pure and substituted iron oxyhydroxides by small-polaron migration," *J Chem Phys,* vol. 140, no. 23, p. 234701, Jun 21 2014.

[72] Y. Li *et al.*, "Oxygen vacancy-rich MoO3−x nanobelts for photocatalytic N2 reduction to NH3 in pure water," *Catalysis Science & Technology,* 10.1039/C8CY02357C vol. 9, no. 3, pp. 803-810, 2019.

[73] J. Lee *et al.*, "Phase-selective active sites on ordered/disordered titanium dioxide enable exceptional photocatalytic ammonia synthesis," *Chemical Science,* 10.1039/D1SC03223B vol. 12, no. 28, pp. 9619-9629, 2021.

[74] B. Sun, S. Lu, Y. Qian, X. Zhang, and J. Tian, "Recent progress in research and design concepts for the characterization, testing, and photocatalysts for nitrogen reduction reaction," *Carbon Energy,* vol. 5, no. 3, p. e305, 2023/03/01 2023.

[75] B.-H. Wang *et al.*, "Recent advances in tunable metal–support interactions for enhancing the photocatalytic nitrogen reduction reaction," *EES Catalysis,* 10.1039/D3EY00191A vol. 2, no. 1, pp. 180-201, 2024.

[76] S. Xiong *et al.*, "One-step preparation of well-dispersed spindle-like Fe2O3 nanoparticles on g-C3N4 as highly efficient photocatalysts," *Ecotoxicology and Environmental Safety,* vol. 208, p. 111519, 2021/01/15/ 2021.

[77] W. Zhang *et al.*, "Novel α-FeOOH Nanorods/Ag3PO4 Semiconductor Composites with Enhanced Photocatalytic Activity and Stability," *Nano,* vol. 11, no. 06, p. 1650071, 2016/06/01 2016.

[78] R. Haounati *et al.*, "Design of direct Z-scheme superb magnetic nanocomposite photocatalyst Fe3O4/Ag3PO4@Sep for hazardous dye degradation," *Separation and Purification Technology,* vol. 277, p. 119399, 2021/12/15/ 2021.

[79] H. Shen, M. Yang, L. Hao, J. Wang, J. Strunk, and Z. Sun, "Photocatalytic nitrogen reduction to ammonia: Insights into the role of defect engineering in photocatalysts," *Nano Research,* vol. 15, no. 4, pp. 2773-2809, 2021.